Exact Frequency-Domain Reconstruction for Thermoacoustic Tomography—II: Cylindrical Geometry

Yuan Xu, Minghua Xu, and Lihong V. Wang*

Abstract—**Microwave-induced thermoacoustic tomography (TAT) in a cylindrical configuration is developed to image biological tissue. Thermoacoustic signals are acquired by scanning a flat ultrasonic transducer. Using a new expansion of a spherical wave in cylindrical coordinates, we apply the Fourier and Hankel transforms to TAT and obtain an exact frequency-domain reconstruction method. The effect of discrete spatial sampling on image quality is analyzed. An aliasing-proof reconstruction method is proposed. Numerical and experimental results are included.**

Index Terms—**Cylindrical, frequency-domain reconstruction, thermoacoustic tomography.**

I. INTRODUCTION

THERMOACOUSTIC tomography (TAT) combines the strength of traditional microwave imaging and ultrasound imaging [1]–[14]. Reviews on TAT and related techniques can be found in [11], [12], [14]. Recently, we derived exact reconstruction algorithms for TAT in both planar and spherical configurations; these are reported in the companion papers [11], [12]. We recognize, however, that in some applications such as the imaging of the limbs, a cylindrical scanning surface may be more appropriate. In this paper, using a new expansion formula in cylindrical coordinates, we derive a frequency-domain reconstruction algorithm [15]–[19] and report our numerical and experimental results in two-dimensional (2-D) cases.

II. METHODS

We assume that the detector scans on a cylindrical surface with a radius of ρ, which encircles all microwave absorbing objects. In our paper, a coordinate with a prime refers to the position in an imaged object, while a coordinate without a prime refers to that of a detector. In the case of thermal confinement,

the temporal spectrum of acoustic field $\overline{p}(\mathbf{r}, k)$ is related to the microwave absorption distribution $\varphi(\mathbf{r}')$ by the following equation [11]:

$$\overline{p}(\mathbf{r}, k) = \frac{i\beta v_s I_0 k \overline{\eta}(k)}{4\pi C} \iiint \varphi(\mathbf{r}') \frac{\exp(-ik|\mathbf{r}-\mathbf{r}'|)}{|\mathbf{r}-\mathbf{r}'|} d\mathbf{r}' \tag{1}$$

where the symbols are defined as in [11]. Cylindrical coordinates are used in the following derivation, where z is shown in [12, Fig. 2], and ρ, ϕ are the polar coordinates within the x–y plane. Following the derivation of the series expansion of $1/|\mathbf{r} - \mathbf{r}'|$ [20], we obtained the following new identity for a series expansion of a spherical wave in a cylindrical coordinate system (see the Appendix for the derivation):

$$\begin{aligned}
&\frac{\exp(-ik|\mathbf{r}-\mathbf{r}'|)}{4\pi|\mathbf{r}-\mathbf{r}'|} \\
&= \frac{-i}{8\pi} \int_{-\infty}^{\infty} dk_z \exp[-ik_z(z'-z)] \\
&\quad \cdot \sum_{m=-\infty}^{\infty} A(m, \mu\rho', \mu\rho) \exp[-im(\phi'-\phi)]
\end{aligned} \tag{2}$$

where $\mu = \text{sgn}(k)\sqrt{|k^2 - k_z^2|}$; $\text{sgn}(\ )$ is the signum function; and A is the function defined as

$$A(m, \mu\rho', \mu\rho) = \begin{cases} J_m(\mu\rho')H_m^2(\mu\rho), & \text{if } |k| \geq |k_z| \\ \dfrac{2i}{\pi} I_m(|\mu|\rho')K_m(|\mu|\rho), & \text{if } |k| < |k_z| \end{cases}$$

where J_m, H_m^2, I_m, and K_m are the mth-order Bessel, second-kind Hankel, and modified Bessel functions, respectively. It has been assumed in the above two equations that $\rho > \rho'$. Substituting (2) into (1) results in

$$\begin{aligned}
\overline{p}(\mathbf{r}, k) = &\frac{\beta v_s I_0 k \overline{\eta}(k) \,\text{sgn}(k)}{8\pi C} \iiint d\mathbf{r}' \varphi(\mathbf{r}') \\
&\cdot \int_{-\infty}^{\infty} dk_z \exp[-ik_z(z'-z)] \\
&\cdot \sum_{m=-\infty}^{\infty} A(m, \mu\rho', \mu\rho) \exp[-im(\phi'-\phi)].
\end{aligned} \tag{3}$$

The $|k| \geq |k_z|$ part of the integration with respect to k_z represents the contribution from the propagation wave, while the $|k| < |k_z|$ part represents the evanescent wave. As the evanescent wave decays rapidly at a distance several wavelengths from

the source, it is not suitable for thermoacoustic imaging. For the case of $|k| \geq |k_z|$, after Fourier transforming both sides of the above equation with respect to ϕ and z, we have

$$\overline{p}_1(m, k_z, k) = \frac{\beta v_s I_0 k \overline{\eta}(k) H_m^2(\mu\rho)}{8\pi C}$$
$$\cdot \int_0^\infty d\rho' \rho' \varphi_1(m, k_z, \rho') J_m(\mu\rho') \quad (4)$$

where $\overline{p}_1(m, k_z, k)$ and $\varphi_1(m, k_z, \rho')$ are the Fourier transforms of $\overline{p}(\mathbf{r}, k)$ and $\varphi(\mathbf{r}')$, respectively. Noticing that the right side of (4) is actually a Hankel transform, an inverse Hankel transform gives

$$\varphi_1(m, k_z, \rho') = \frac{8\pi C}{\beta v_s I_0} \int_0^\infty d\mu \frac{\mu \overline{p}_1(m, k_z, k) J_m(\mu\rho')}{k \overline{\eta}(k) H_m^2(\mu\rho)},$$
$$|k| \geq |k_z|.$$

Applying a variable change of the integral variable from μ to k to the above equation results in

$$\varphi_1(m, k_z, \rho') = \frac{8\pi C}{\beta v_s I_0} \int_{k_z}^\infty dk \frac{\overline{p}_1(m, k_z, k) J_m(\mu\rho')}{\overline{\eta}(k) H_m^2(\mu\rho)},$$
$$|k| \geq |k_z|. \quad (5)$$

At last, $\varphi_1(m, k_z, \rho')$ is inversely Fourier transformed with respect to m and k_z to yield $\varphi(\phi', z', \rho')$. Equation (5) gives an exact mapping relation between the spectrum of the collected signals and the spectrum of the distribution of microwave energy deposition and is the essence of our reconstruction method.

An exact reconstruction method for ultrasonic reflectivity imaging with a cylindrical scanning surface was given in [16]. However, our results are much simpler and more stable. In their equation A24, $J_m(\mu r_0)$, where r_0 is the radius of the scanning cylindrical surface, appeared in the denominator and can be zero for some values of μ; consequently, this term can cause instability. In our (5), $H_m^2(\mu\rho)$ appeared in the denominator, which cannot be zero for a finite μ.

To summarize, the reconstruction procedure consists of the following steps.

1) The signal from the detector $p(\phi, z, \overline{t})$ is Fourier transformed with respect to $\overline{t}$ to yield $\overline{p}(\phi, z, k)$. Deconvolution with respect to the finite pulse length can be implemented immediately after the Fourier transform.
2) $\overline{p}(\phi, z, k)$ is Fourier transformed with respect to z and ϕ, giving $\overline{p}_1(m, k_z, k)$.
3) According to (5), $\overline{p}_1(m, k_z, k)$ is mapped to $\varphi_1(m, k_z, \rho')$.
4) $\varphi_1(m, k_z, \rho')$ is inversely Fourier transformed with respect to m, k_z to yield $\varphi(\phi', z', \rho')$.

III. RESULTS AND DISCUSSION

To test our method, images from both numerically simulated and experimental data were reconstructed in a 2-D case. We chose the 2-D case rather than the three-dimensional (3-D) case to reduce the computational and experimental complexity. For the 2-D case, the reconstruction equation can be derived from
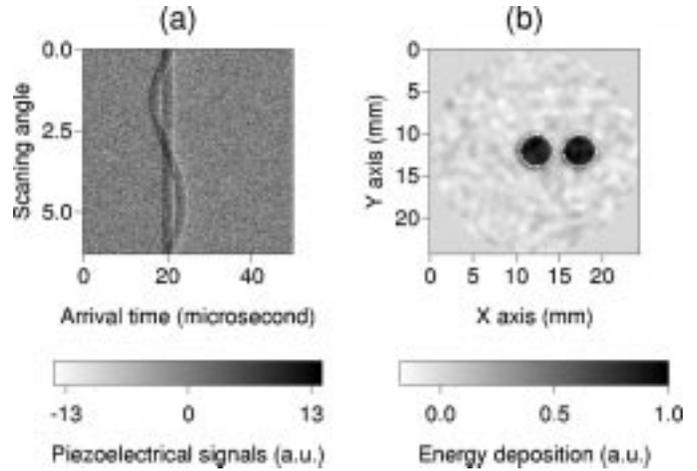
Fig. 1. The images (a) before and (b) after the reconstruction from the simulated data of two cylinders.
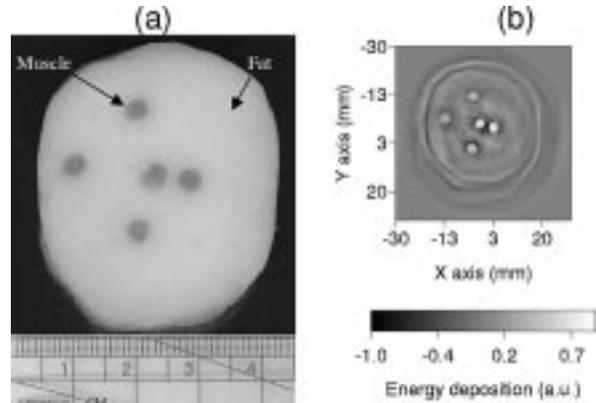
Fig. 2. (a) The cross section of a fat sample containing 5 pieces of muscle cylinders. (b) The reconstructed image from the experimental data.

(4) by replacing all k_z with zero. The extension of the conclusions of the 2-D case to a 3-D one is straightforward.

A. Numerical Simulation

The thermoacoustic imaging of two cylinders was numerically simulated, where the radius of each cylinder was 2 mm; the distance between the centers of the cylinders was 5 mm; and the center of one of the cylinders was positioned at the origin of the circle of detection. Cylinders were chosen because the analytical expression for their thermoacoustic signal is available [21]. In the simulations, the temporal-frequency range was from about 0 to 2 MHz, which was close to our experimental situation [14]. For the noiseless simulated data, the reconstruction is almost perfect. Therefore, we show only the results from noisy data. Fig. 1 shows the images before and after the reconstruction from the simulated data with introduced additive noise. The units for the signals and energy deposition in Figs. 1 and 2 are relative ones. Calibration of our system is needed to obtain an absolute measurement. The radius of the circle of detection was 30 mm; the angular scanning range was 2π with 256 steps; and the thermoacoustic signals were sampled for 50 μs at a sampling rate of 4 MHz. The signal-noise-ratio (SNR) of the raw data shown in Fig. 1(a) was 1. The reconstructed image shown in Fig. 1(b) is in good agreement with the real objects, whose

outlines are plotted as dotted circles in Fig. 1(b). The dimensions of the reconstructed cylinders are 4 mm along both the x and the y directions. The SNR of the reconstructed image is about 8, which is improved greatly compared with that of the raw data.

B. Experiment Results

The experimental setup for 2-D TAT in a cylindrical configuration is the same as that in [12]. The sample is shown in Fig. 2(a), which was photographed after the experiment. Microwave pulses were delivered to the sample from below. The imaging plane was 2 cm above the bottom of the tissue sample. Above the plane, there is another layer of fat about 1 cm thick. The sample consisted of five muscle cylinders with a diameter of about 3 mm and a height of 6 mm. The muscle cylinders were surrounded by pork fat. The electrical property of interest to this imaging technique is the microwave attenuation coefficient of the medium at the experimental microwave frequency, 3 GHz. The microwave attenuation coefficients of fat and muscle are $9\ \mathrm{cm}^{-1}$ and $1\ \mathrm{cm}^{-1}$, respectively. The microwave absorption in mineral oil can be neglected, compared with the absorption in fat and muscle. During the experiment, the transducer scanned around the sample at a radius of 7.1 cm from $0°$ to $360°$ with a step size of $2.25°$. The thermoacoustic signals were sampled for 60 μs at a sampling rate of 20 MHz. The time between the end of a microwave pulse and the acquisition of the thermoacoustic signal was between 10 μs and 20 μs in our system, depending on the distance of the transducer to the nearest sample surface.

Fig. 2(b) shows the reconstructed image from the experimental data. The reconstructed image is in good agreement with the real objects. The boundaries between the fat and the surrounding medium and the muscle cylinders are imaged clearly. However, it can be seen that the quality of the image decreases with the increasing distance of the objects from the center of the circle of detection. One possible reason is that the finite surface area of the detector, which has a 6-mm diameter in this experiment, may cause blurring of the image perpendicular to the radial direction, and this blurring is more serious when the object is farther from the center. Another possible reason is that the microwave field decreases when the radius increases in our irradiation configuration.

Our method can be applied to analyze the effect of the discrete sampling by the detector along the circle of detection on imaging. This can be illustrated by analyzing the signals from a point source located at radius ρ_1. According to (4)

$$\overline{p}_1(m, k) \propto J_m(k\rho_1). \qquad (6)$$

Fig. 3 shows how $J_m(k\rho_1)$ changes with m, where $k = 8.37\ \mathrm{mm}^{-1}$ (the wave number of a 2-MHz acoustic wave) and $\rho_1 = 10$ mm. It is clear that $J_m(k\rho_1)$ has considerable value until $m \approx k\rho_1$, where the Bessel function makes a transition from near-field behavior to far-field behavior. Therefore, it is safe to claim that, with respect to variable ϕ, $\overline{p}(\mathbf{r}, k)$ is band-limited by $k\rho_1$. According to the Nyquist criteria, the number of scanning points per cycle should be at least $2k\rho_1$ to avoid aliasing. In other words, for a fixed number of scanning points N, the maximum wave number before aliasing occurs
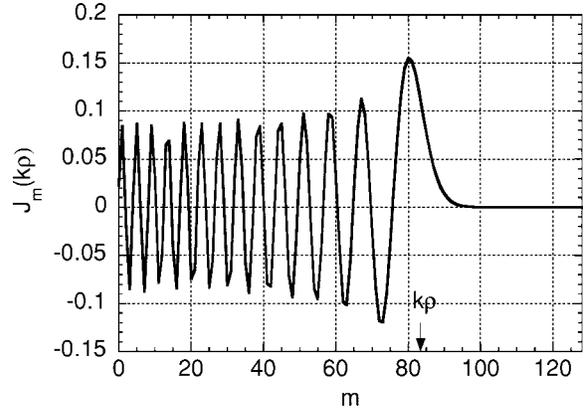
Fig. 3. $J_m(k\rho_1)$ versus m, where $k = 8.37$ mm^{-1} (the wave number of a 2 MHz acoustic wave) and $\rho_1 = 10$ mm.

is $k_{\max} \approx N/(2\rho_1)$. It can be seen that the maximum wave number is inversely proportional to ρ_1. For the same N and temporal spectrum of signal, the aliasing may be more serious for signals coming from sources at a greater radial distance than for those closer to the center. The above analysis also points out a way to produce an aliasing-free image from the data obtained by discrete detection. That is to apply a filter in the temporal-frequency domain to the spectrum of the temporal data with a stopband at about $N/(2\rho_{\max})$, where $\rho_{\max}$ is the maximum radius of imaging range of interest. The application of the filter will decrease the resolution of the image; however, it can guarantee that there will be no aliasing in the image.

C. Discussion

Since our method is implemented in the frequency domain using the fast Fourier transform (FFT) technique, the computational efficiency is much greater than if implemented in the time domain. The most time-consuming computation in the numerical reconstruction lies in (5), which is a Hankel transform. Fortunately, a quasi-fast algorithm for it, which is as efficient as a one-dimensional FFT, is available [22]. Following the methods in [11], our method can explicitly include and further eliminate the effect of many limitations from the experiment, such as the finite size of the detector surface, the microwave pulse length, and the finite response frequency range of the detector. Additionally, combining our method and the techniques in [16], a new exact reconstruction algorithm for 3-D ultrasonic reflectivity imaging with a cylindrical aperture can be derived. Finally, we would like to point out that the reconstruction methods reported in this paper and the two companion papers [11], [12] are also applicable to photoacoustic or optoacoustic tomography as well as other diffraction-based inverse source problem.

The size of tissue samples that can be imaged by our system is mainly limited by the safety standard on microwave power, the microwave frequency, the microwave irradiation configuration, the sensitivity of the ultrasonic transducer, the dynamic range of the preamplifier and sampling system, and the affordable imaging time. The effect of microwave frequency on the imaging depth was addressed in reference [13]. A microwave irradiation configuration that renders a uniform microwave irradiation within the sample will also increase the capacity of the system to image larger samples. A large dynamic range of the

preamplifier and the sampling system is necessary to accurately collect the thermoacoustic signals from both the surface and the inside of a sample. A more sensitive ultrasonic transducer and a longer imaging time can improve the signal-to-noise ratio of acoustic signals and make the weak signals from the inside of large samples detectable.

In our initial computation, the reconstruction of a single 2D image required about 2 min in a Dell Precision 330 computer (Intel Pentium 4 processor with a clock frequency of 1.5 GHz) with Matlab programs if there was no precomputation of Bessel and Hankel functions. However, our initial computation was aimed at verifying the proposed algorithm rather than demonstrating the computation efficiency. The proposed algorithm can be implemented with high computational efficiency as stated in the discussion section. For high computational efficiency, the program should be coded with languages such as C or Fortran, Bessel and Hankel functions should be precomputed, and the fast Hankel transform algorithm should be adopted. The evaluation of the computation efficiency of our algorithm is a topic for future studies.

IV. CONCLUSION

Using a new expansion of a spherical wave in the cylindrical coordinate system, we applied the Fourier transform and Hankel transform techniques to TAT with a cylindrical detection surface. The reconstruction algorithm is verified by both numerical simulations and experimental results in 2-D cases. The method was applied to analyze the effect of discrete sampling by the detector along the circle of detection on imaging; an aliasing-free reconstruction method for discrete sampling along the azimuth direction is proposed.

APPENDIX

The derivation of (2) will be presented here. The spherical wave $G_k(\mathbf{r}, \mathbf{r}') = \exp(-ik|\mathbf{r} - \mathbf{r}'|)/(4\pi|\mathbf{r} - \mathbf{r}'|)$ is a solution to the wave equation with a point source

$$\nabla_r^2 G_k(\mathbf{r}, \mathbf{r}') + k^2 G_k(\mathbf{r}, \mathbf{r}') = -\delta(\mathbf{r} - \mathbf{r}'). \quad (A1)$$

The solution can be expanded in terms of orthonormal functions of z and ϕ in a cylindrical coordinate system

$$G_k(\mathbf{r}, \mathbf{r}) = \left(\frac{1}{2\pi}\right)^2 \sum_{m=-\infty}^{\infty} \int_{-\infty}^{\infty} dk_z g_m(k, k_z, \rho, \rho') \\ \cdot \exp[im(\phi - \phi') + ik_z(z - z')]. \quad (A2)$$

Substituting (A2) into (A1) results in an equation for the radial Green's function g_m

$$\frac{1}{\rho} \frac{d}{d\rho} \left(\rho \frac{dg_m}{d\rho}\right) + \left(k^2 - k_z^2 - \frac{m^2}{\rho^2}\right) g_m = -\frac{\delta(\rho - \rho')}{\rho}. \quad (A3)$$

When $|k| < |k_z|$, following the derivation of the series expansion of $1/|\mathbf{r} - \mathbf{r}'|$ [20], one obtains a similar expansion for the spherical wave

$$g_m = I_m(|\mu|\rho')K_m(|\mu|\rho). \quad (A4)$$

We next consider the case of $|k| \geq |k_z|$ and $k > 0$. Noticing that when $\rho \to \infty$, g_m behaves asymptotically as $\exp[-i\mu(\rho - \rho')]$ ($\rho > \rho'$ is implicit in our model), one can follow the derivation in [20] and obtain

$$g_m = \frac{\pi}{2i} J_m(\mu\rho')H_m^2(\mu\rho). \quad (A5)$$

Similarly, for $|k| \geq |k_z|$ and $k < 0$

$$g_m = \frac{\pi i}{2} J_m(|\mu|\rho')H_m^1(|\mu|\rho). \quad (A6)$$

Using the following identities of Bessel and Hankel functions [23]:

$$H_m^1(\mu\rho) = -(-1)^m H_m^2(-\mu\rho),$$

$$J_m(\mu\rho) = (-1)^m J_m(-\mu\rho)$$

and combining (A2) and (A4)–(A6), we obtain (2).

REFERENCES

[1] W. Joines, R. Jirtle, M. Rafal, and D. Schaeffer, "Microwave power absorption differences between normal and malignant tissue," *Radiation Oncol. Biol. Phys.*, vol. 6, pp. 681–687, 1980.

[2] S. Chaudhary, R. Mishra, A. Swarup, and J. Thomas, "Dielectric properties of normal human breast tissues at radiowave and microwave frequencies," *Indian J. Biochem. Biophys.*, vol. 21, pp. 76–79, 1984.

[3] W. Joines, Y. Zhang, C. Li, and R. Jirtle, "The measured electrical properties of normal and malignant human tissues from 50–900 MHz," *Med. Physics*, vol. 21, pp. 547–550, 1994.

[4] L. E. Larsen and J. H. Jacobi, Eds., *Medical Applications of Microwave Imaging.* Piscataway, NJ: IEEE Press, 1986.

[5] S. Caorsi, A. Frattoni, G. L. Gragnani, E. Nortino, and M. Pastorino, "Numerical algorithm for dielectric-permittivity microwave imaging of inhomogeneous biological bodies," *Med. Biol. Eng. Comput.*, vol. NS-29, pp. 37–44, 1991.

[6] M. S. Hawley, A. Broquetas, L. Jofre, J. C. Bolomey, and G. Gaboriaud, "Microwave imaging of tissue blood content changes," *J. Biomed. Eng.*, vol. 13, pp. 197–202, 1991.

[7] P. M. Meaney, K. D. Paulsen, and J. T. Chang, "Near-field microwave imaging of biologically-based materials using a monopole transceiver system," *IEEE Trans. Microwave Theory Tech.*, vol. 46, pp. 31–45, Jan. 1998.

[8] R. A. Kruger, P. Liu, Y. R. Fang, and C. R. Appledorn, "Photoacoustic ultrasound (PAUS)-reconstruction tomography," *Med. Phys.*, vol. 22, pp. 1605–1609, 1995.

[9] C. G. A. Hoelen, F. F. M. Demul, R. Pongers, and A. Dekker, "Three-dimensional photoacoustic imaging of blood vessels in tissue," *Opt. Lett.*, vol. 23, pp. 648–650, 1998.

[10] G. Ku and L.-H. V. Wang, "Scanning thermoacoustic tomography in biological tissue," *Med. Phys.*, vol. 27, pp. 1195–1202, 2000.

[11] Y. Xu, D. Feng, and L.-H. V. Wang, "Exact frequency-domain reconstruction for thermoacoustic tomography—II: Planar geometry," *IEEE Trans. Med. Imag.*, vol. 21, no. 7, pp. 823–828, July 2002.

[12] M. Xu and L.-H. V. Wang, "Time-domain reconstruction for thermoacoustic tomography in a spherical geometry," *IEEE Trans. Med. Imag.*, vol. 21, no. 7, pp. 814–822, July 2002.

[13] G. Ku and L.-H. V. Wang, "Scanning microwave-induced thermoacoustic tomography: Signal, resolution, and contrast," *Med. Phys.*, vol. 28, pp. 4–10, 2001.

[14] Y. Xu and L.-H. V. Wang, "Signal processing in scanning thermoacoustic tomography in biological tissues," *Med. Phys.*, vol. 28, pp. 1519–1524, 2001.

[15] H. Stark, J. W. Woods, I. Paul, and R. Hingorani, "Direct Fourier reconstruction in computer tomography," *IEEE Trans. Acoust. Speech Signal Processing*, vol. ASSP-29, pp. 237–245, 1981.

[16] S. J. Nortan and M. Linzer, "Ultrasonic reflectivity imaging in three dimensions: Exact inverse scattering solution for plane, cylindrical and spherical aperture," *IEEE Trans. Biomed. Eng.*, vol. BME-28, pp. 202–220, 1981.

[17] K. Nagai, "A new synthetic-aperture focusing method for ultrasonic b-scan imaging by the Fourier transform," *IEEE Trans. Sonics Ultrason.*, vol. SU-32, pp. 531–536, 1985.

[18] J. Lu, "Experimental study of high frame rate imaging with limited diffraction beams," *IEEE Trans. Ultrason. Ferroelect. Freq. Contr.*, vol. 45, pp. 84–97, Jan. 1998.

[19] S. X. Pan and A. C. Kak, "A computational study of reconstruction algorithms for diffraction tomography: Interpolation versus filtered backprojection," *IEEE Trans. Acous. Speech Signal Processing*, vol. ASSP-31, pp. 1262–1275, 1983.

[20] J. D. Jackson, *Classical Electrodynamics*.   New York: Wiley, 1975.

[21] G. J. Diebold, M. I. Khan, and S. M. Park, "Photoacoustic signatures of particulate matter: Optical production of acoustic monopole radiation," *Science*, vol. 250, pp. 101–104, 1990.

[22] A. E. Siegman, "Quasi fast Hankel transform," *Opt. Lett.*, vol. 1, pp. 13–15, 1977.

[23] M. Abramowitz and I. A. Stegun, *Handbook of Mathematical Functions*.   New York: Dover, 1972.